Available online at www.sciencedirect.com
ScienceDirect
Trans. Nonferrous Met. Soc. China 33(2023) 3487−3502

Transactions of Nonferrous Metals Society of China
www.tnmsc.cn

Failure characteristics and energy distributions of surrounding rock in hard rock tunnels subjected to different three-dimensional stress conditions

Ming TAO[1], Rui ZHAO[1], Hua-tao ZHAO[1], Yi-qing WANG[1], Wen-zhuo CAO[2], Shao-feng WANG[1]

1. School of Resources and Safety Engineering, Central South University, Changsha 410083, China;
2. Royal School of Mines, Imperial College, London, United Kingdom

Received 4 April 2022; accepted 15 August 2022

Abstract: To study the failure characteristics of surrounding rock near an excavated tunnel under different three-dimensional stress conditions, a TRW3000 rock true triaxial electro-hydraulic servo mutagenesis testing system was used to conduct triaxial loading experiments on granite specimens with a circular hole. A high-definition micro-camera system was used to record the failure process near the circular hole. The results show that spalling failure occurs near the holed specimen under low-stress conditions, and rockburst appears around the holed specimen under high-stress conditions. Increasing the horizontal stress can prevent the occurrence of rockburst. The evolution of strain energy density (SED) in the surrounding rock of the holed specimen under different stress conditions was simulated. The findings show that the distribution of SED around the circular hole decreases with an increase in horizontal stress. The SED distributions around the circular hole are basically consistent with the damage distributions in the experiments, namely, butterfly-shaped, ear-shaped, and ring-shaped.

Key words: deep hard rock tunnel; true triaxial experiment; horizontal stress difference; failure characteristics; energy distribution

---

1 Introduction

Underground engineering failures gradually increase as the number of underground constructions, such as traffic tunnels, mines, laboratories, and civil defense structures, increases. These underground constructions are often influenced by geo-stress, external disturbances, and other factors in the underground space and experience unconventional failures, such as spalling, rockburst, excavation damaged zones, and zonal disintegration [1−7]. Failure often causes casualties, equipment damage, and delays, bringing significant potential safety hazards to the construction of deep hard rock projects [8−11]. Therefore, the failure of surrounding rock and its influencing factors should be investigated for underground engineering and rock mechanics.

Several researchers have conducted a series of investigations to study the failure characteristics and stability of underground tunnels. MARTINI et al [12] reported that spalling failure induced V-shaped failure zones in surrounding rock. FENG et al [13] demonstrated that the spalling failure was parallel to the excavated surfaces of the tunnel and was influenced by the tunnel’s shape and the orientation of the principal stress. SI et al [14] studied the spalling failure around D-shaped and circular tunnels under three-dimensional stress states and showed that an evident spalling failure occurred at the sidewalls of the tunnels. Other related studies on spalling failures near underground tunnels are available [15−19].

Rockburst is another common damage that occurs in the underground tunnels, which was firstly

---

Corresponding author: Hua-tao ZHAO, Tel: +86-18711093389, E-mail: huatao_zhao@163.com

DOI: 10.1016/S1003-6326(23)66349-6

recorded in the early 1990s in the Witwatersrand Gold Mine in South Africa [20]. Subsequently, several investigations on rockburst have been conducted. DYSKIN and GERMANOVICH [21] studied the mechanism of rockburst caused by crack propagation on the free surface of a tunnel using a two-dimensional model. ORTLEPP and STACEY [22] classified rockburst into strain rockburst, buckling, face crush/pillar burst, shear rupture, and fault-slip burst after many investigations and considered strain rockburst to be the most common rockburst in underground tunnels. Furthermore, a few studies have shown that rockburst is related to the coupling effect of geo-stress and external dynamic disturbances [9,23−26].

Although spalling failure and rockburst are two different failure phenomena in underground tunnels, they are strongly correlated [2]. DU et al [27] verified that spalling cracks are the precursors to rockburst. GONG et al [28] determined that the mechanism of rockburst induced by spalling is mainly embodied in promoting large buckling deformation and weakening the rock's strength. The aforementioned studies focused on revealing spalling failure, rockburst, and their evolutionary process around an underground tunnel; however, limited studies have been conducted on the specific reasons for spalling, rockburst, and their influencing factors. Therefore, experimental tests should be conducted to investigate the failure process and obtain the relationship between the three-dimensional (3D) stress state of the surrounding rock and the occurrence of spalling and rockburst as well as the influence of stress on the stability of underground tunnels.

In this study, the failure characteristics of holed specimens under different stress conditions were tested using a true triaxial testing machine. Based on the experimental records, the evolution process and failure mechanism of an underground tunnel under 3D stress conditions, as well as the relationships between the stress conditions and failure modes of the surrounding rock, were first analyzed. Subsequently, the distributions of energy and their evolutionary process in the vicinity of a circular tunnel under different stress states were numerically studied using ABAQUS. The findings of this study can provide a reference and basis for supporting the design and prevention of disasters in underground tunnels.

2 Experimental

2.1 Specimen preparation

The specimens were grey-white porphyry granite taken from the whole rock to ensure the same physical properties and make the experimental results comparable. To simulate 3D stress in deep hard rock, the specimens were machined into cubes of 100 mm × 100 mm × 100 mm in length, width, and height, respectively. The surfaces were polished using a grinder, and the processing accuracy strictly followed the standards of the International Society for Rock Mechanics and Rock Engineering (ISRM). The flatness of each surface was controlled to be 0.05 mm, and the vertical deviation of adjacent surfaces was 0.25°. A cylindrical hole with a diameter of d=25 mm was prefabricated in the central part of the specimen, as shown in Fig. 1. The uniaxial compressive strength (UCS) of the intact rock specimen was 98 MPa, and Poisson's ratio was 0.25.

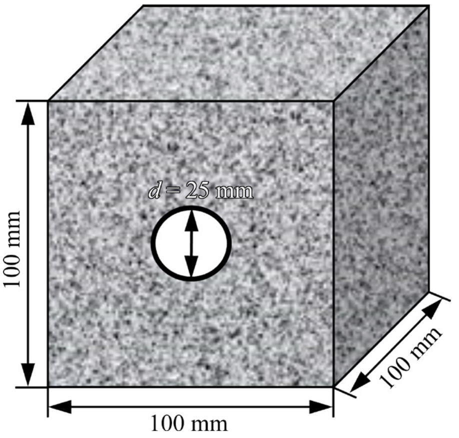

Fig. 1 Schematic diagram of cubic granite specimen used in present study

2.2 Experimental equipment

The experiment was conducted on a TRW3000 rock true triaxial electro-hydraulic servo mutagenesis testing system, as shown in Fig. 2(a). The maximum loads in the x, y, and z directions were 2000, 2000, and 3000 kN, respectively. The loading rates in the x, y, and z directions were controlled within 10−10000 N/s. The measurement ranges of the displacement in the x, y, and z directions were 0−200, 0−100, and 0−100 mm, respectively. The measurement accuracy and resolution were higher than 0.5% and 0.001 mm, respectively, in all three directions. During the loading process, a high-definition (HD) micro-camera system, as shown in Fig. 2(b), was used to record the failure near the sidewalls of the hole in real time and to synchronously transmit the experimental results to the computer.

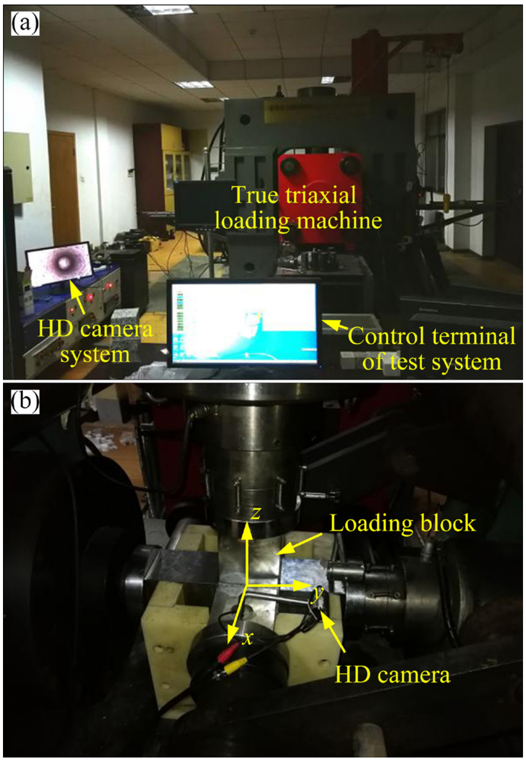

Fig. 2 TRW3000 rock true triaxial electro-hydraulic servo mutagenesis test system (a) and loading diagram of rock specimens (b)

2.3 Experimental methods and schemes

A cylindrical hole with a diameter of 25 mm was machined on the loading block of the x-axis, and an HD micro-camera was installed in the circular hole. The axial direction of the hole coincided with the loading direction of the x axis. The serial numbers of the specimens are summarised in Table 1, where the three words in the specimen number represent the stresses in the x, y, and z directions, respectively. To construct the 3D stress state in the underground space, the stresses are loaded along the x, y, and z axes, and the corresponding stresses are listed in Table 1. The symbols ⇧ represent the stress variation in the z direction when a through crack is formed in the sidewalls of the hole.

The specimens were divided into four groups, as listed in Table 1. The first group included 5-10-σ_z, 10-20-σ_z, 10-30-σ_z, and 10-40-σ_z, which were used to investigate the influence of the horizontal stress difference on the failure characteristics of the specimens. Based on the study by STEPHANSSON et al [29], 5-10-σ_z and 10-20-σ_z can be considered to correspond to the stress conditions around shallowly buried tunnels ($h < 400$ m), and 10-30-σ_z and 10-40-σ_z are the simulations of the stress conditions around deep tunnels ($h > 800$ m). The second group included 10-20-σ_z and 30-40-σ_z, which were used to study the failure characteristics of the specimen under the same horizontal stress difference, including shallow and deep stress conditions. The purpose of the third group was to investigate the influence of the stress along the axial direction of the hole on the failure characteristics of the specimen under high-stress conditions. The last group, 0-0-σ_z, was used to obtain the UCS values of the holed specimens.

Table 1 Stress condition of surrounding rock corresponding to specimen number

Group No.	Specimen number	σ_x/MPa	σ_y/MPa	σ_z/MPa
1	5-10-σ_z	5	10	⇧
	10-20-σ_z	10	20	⇧
	10-30-σ_z	10	30	⇧
	10-40-σ_z	10	40	⇧
2	10-20-σ_z	10	20	⇧
	30-40-σ_z	30	40	⇧
3	10-40-σ_z	10	40	⇧
	30-40-σ_z	30	40	⇧
	50-40-σ_z	50	40	⇧
4	0-0-σ_z	0	0	⇧

After the specimen was installed in the triaxial test machine, the HD micro-camera system was opened. The stresses applied by the x, y, and z axes of the triaxial testing machine were preset to the target values, namely, the serial number of the specimen. The specimen was loaded by the x, y, and z axes simultaneously, and the loading rate was 500 N/s (0.05 MPa/s). The stresses in the x and y axes were firstly loaded to the target value using stress control and remained constant. Then, the stress along the z axis was continuously loaded to 600 kN (60 MPa), and the loading method was changed to displacement control. The loading rate was controlled to 0.15 mm/min and loading was stopped once a penetrating crack occurred near the sidewalls of the hole. The triaxial strength of the holed specimen increases with the increase of the minimum and intermediate principal stresses, and the increments gradually decrease as the minimum and intermediate principal stresses exceed 30 MPa.

3 Results and discussion

3.1 Failure characteristics of holed specimens under different stress conditions

The recordings indicated that the failure characteristics of the holed specimen were consistent when the specimens were loaded to the stress conditions of shallowly buried tunnels. A small number of rock fragments appeared on the sidewalls of the specimens, as shown in Fig. 3(a). In this case, the failure processes around shallowly buried tunnels can be divided into four periods: quiet, debris ejection, crack propagation, and rock fragment exfoliation. During the quiet period, the microfractures in the specimen are compacted, and no evident failure is observed in the sidewalls of the hole. During this period, strain energy begins to accumulate in the rock specimen, particularly in the vicinity of the circular hole. This period lasts for approximately 15 min. The specimen failure enters the debris ejection period as the maximum principal stress increases, small debris is gradually ejected from the right side of the hole, and the ejection trajectory is a parabola. Part of the strain energy in the surrounding rock is gradually released as the debris is ejected from the circular hole. This period lasts for 7−8 min. With an increase in the stress environment, the velocity of debris ejection increases, the volume of debris also increases, and the entire process lasts for 4−5 min. Under the action of compressive stress, tensile cracks gradually appear in the damaged area caused by particle ejection. After the crack propagation period, there is a quiet period, which means that the surrounding rock enters the stage of strain accumulation again. During the rock fragment exfoliation period, rock pieces near the cracks caused by debris ejection gradually exfoliate from the sidewalls, and a small number of rock fragments begin to bulge from the inner wall, resulting in spalling failure. As the maximum principal stress continuously increases, the rock fragment exfoliation extends from the middle parts to both ends along the axial direction of the hole until a through crack is formed near the inner wall of the hole and loading is stopped. The size and number of rock fragments are larger than those in the last period, and the failure that occurs in the right sidewall is always greater than that on the left side during this process. The entire process, including the short quiet period and rock fragment exfoliation period, lasts for 6−7 min.

Severe failure occurs near both sidewalls of the hole as high stress acts on the specimen, namely, 10-40-σ_z, as shown in Fig. 3(b). This can be regarded as the case for a tunnel in a deep area. Their failure processes are similar; however, a certain difference can be found in contrast to that in the low-stress state. Specifically, the specimen failure enters the crack propagation period rapidly without evident debris ejection after the quiet period, which means that there is no debris ejection period in such a stress environment. Subsequently, the rock fragment starts to bulge from the inner wall after a brief quiet period and then gradually heaves up until spalling, which is similar to the rock fragment exfoliation period in the low-stress state. This indicates that the release rate of strain energy in the deep surrounding rock is faster and intenser than that in the shallow surrounding rock. The entire process lasts for 5−6 min. As the maximum principal stress increases, the failure of the specimen becomes stronger; further, some small rock debris is first ejected from the inner wall of the circular hole, and then several large rock fragments peel off rapidly from the sidewalls, which last for 2−3 min. This is because a large amount of elastic strain energy is stored in the specimen and in the vicinity of the hole in a high-stress environment, which can lead to a rapid release of strain energy and cause a violent rockburst around the hole if the surrounding rock is damaged. Therefore, the failure processes around the deep tunnel can be divided into quiet, crack propagation, rock fragment exfoliation, and rockburst periods.

The failure process of Specimen 50-40-σ_z is similar to that of Specimen 10-40-σ_z, with four periods, including the quiet period, crack propagation period, rock fragment exfoliation period, and rockburst period, which can be seen during loading processes, as shown in Fig. 3(c). Initially, the specimen is quiet for approximately 30 min. Subsequently, tensile crack propagation occurs near the sidewalls. After a quiet period, the

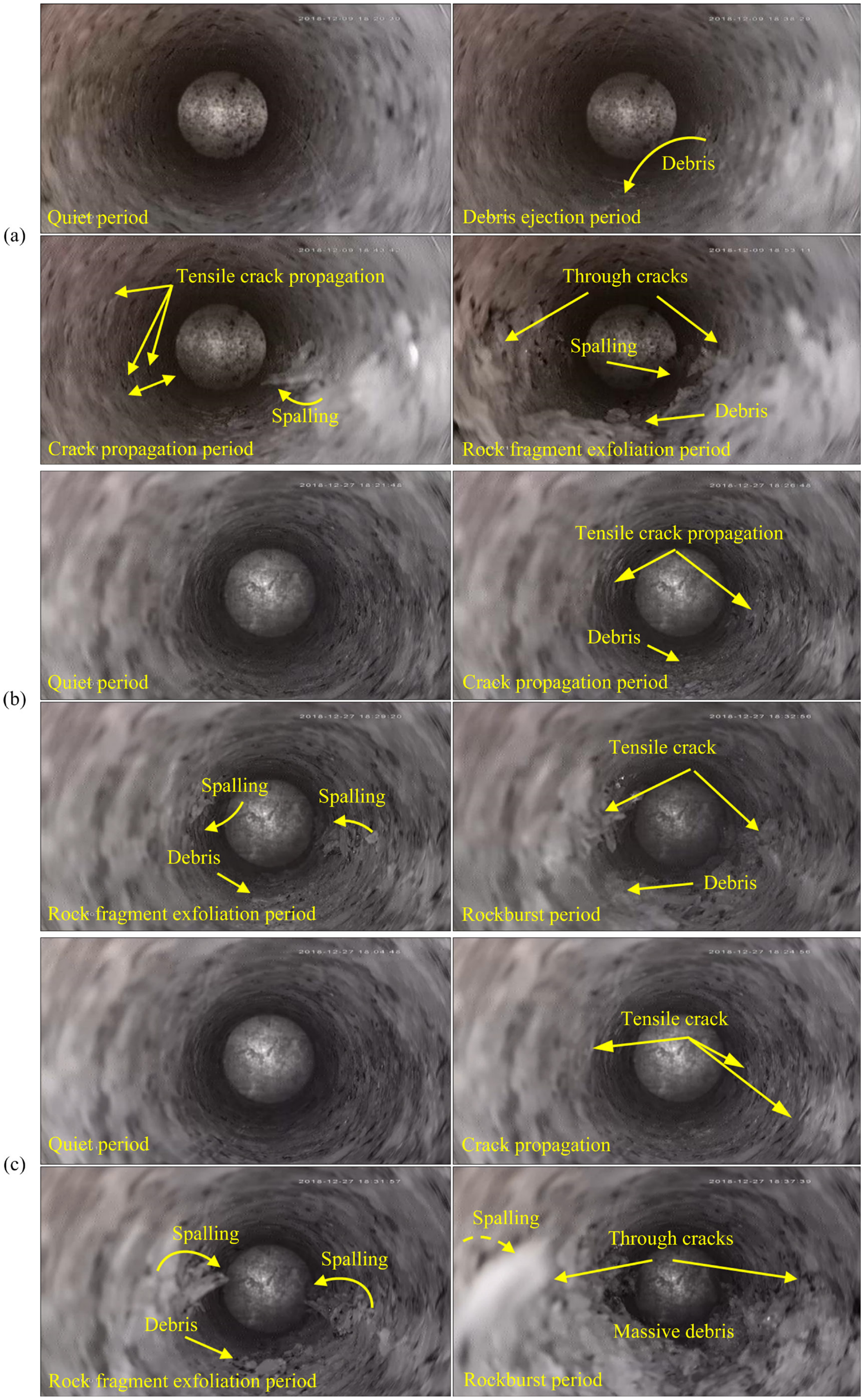

Fig. 3 Failure process of specimen under different stress conditions: (a) 10-20-σ_z; (b) 10-40-σ_z; (c) 50-40-σ_z

rock fragments gradually peel off from the sidewalls. With an increase in the maximum principal stress, the spalling speed increases and the failure area penetrates along the axial direction of the hole. The spalling period lasts for 2−3 min, and then rockburst occurs simultaneously on both sidewalls of the hole. Several rock fragments are suddenly and violently ejected toward the tunnel surface, and the rock powder is ejected to form a dust mist. The entire rockburst process lasts for approximately 30 s, and there is no evident phenomenon after the stress is maintained for a while and the loading is stopped. In contrast to Specimen 10-40-σ_z, the stability of the surrounding rock mass and the strength of the holed specimen increase significantly; however, the severity of the surrounding rock failure is significantly enhanced.

Specimens 10-20-σ_z and 10-30-σ_z were considered as examples to display the failure characteristics near the sidewalls of the hole after spalling and rockburst, respectively. Figure 4 shows that the V-shaped crack formed by rockburst under high-stress conditions is deeper and wider than that formed by spalling failure under low-stress conditions. The through V-shaped crack is perpendicular to the maximum principal stress (σ_z), which is consistent with actual engineering and previous studies [28,30].

To better describe and reveal the failure mechanism of rockburst in the surrounding rock, a diagram sketch of the failure processes and mechanisms is plotted in Fig. 5. In the quiet period, microcracks in the rock surrounding the circular hole expand along with the maximum principal stress (σ_z) owing to the compressive stress concentration that occurs on both sidewalls of the hole, as shown in Fig. 5(a). During the crack propagation period, the microcracks gradually expand and coalesce with other microcracks to form tensile cracks, and the rock fragment is ejected if the crack extends to the middle part of the sidewalls, as shown in Fig. 5(b). During the rock fragment exfoliation period, internal cracks induce rock fragments on the surface of the circular hole to spall. The damaged area caused by spalling on the sidewalls provides the conditions for more cracks to penetrate the hole wall, which can further provide a free surface for rockburst. During the rockburst period, the elastic strain energy stored in the surrounding rock, particularly in the undamaged surrounding rock, is suddenly released with an increase in the maximum principal stress. The released strain energy is transformed into dissipative energy of rock fragmentation and kinetic energy of fragment ejection. Spalling failure is closely related to the propagation and coalescence of internal tension cracks, and tensile failure dominates the entire rockburst process.

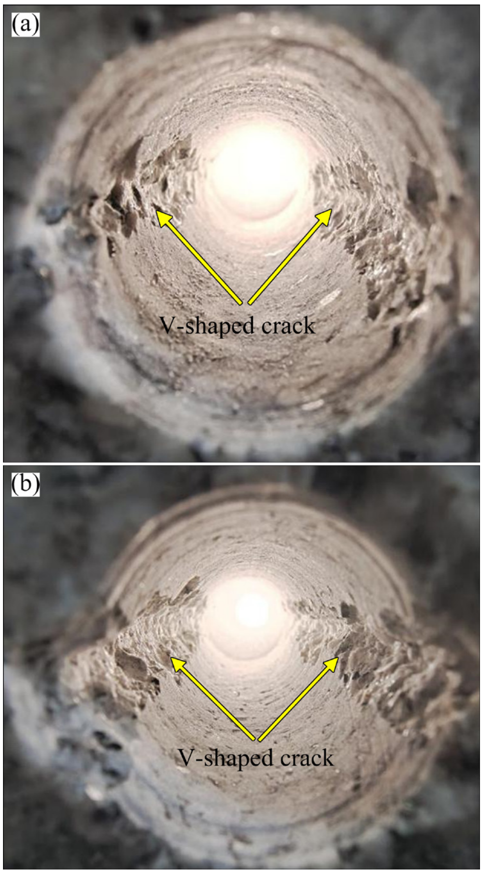

Fig. 4 V-shaped crack process of different specimens: (a) 10-20-σ_z; (b) 10-30-σ_z

3.2 Influence of stress condition on failure of surrounding rock

Generally, severity and failure characteristics are largely dependent on the stress conditions of the surrounding rock. As discussed in the previous section, a large stress can induce more serious damage to the surrounding rock and is more likely to cause rockburst. In practice, the stress loaded on an underground tunnel in the vertical direction generally changes with the buried depth of the tunnel, and the stress at a specific depth is regarded as constant. The stress in the horizontal direction changes frequently because of the influence of tectonic stress. The stability and failure characteristics of the surrounding rock under different horizontal

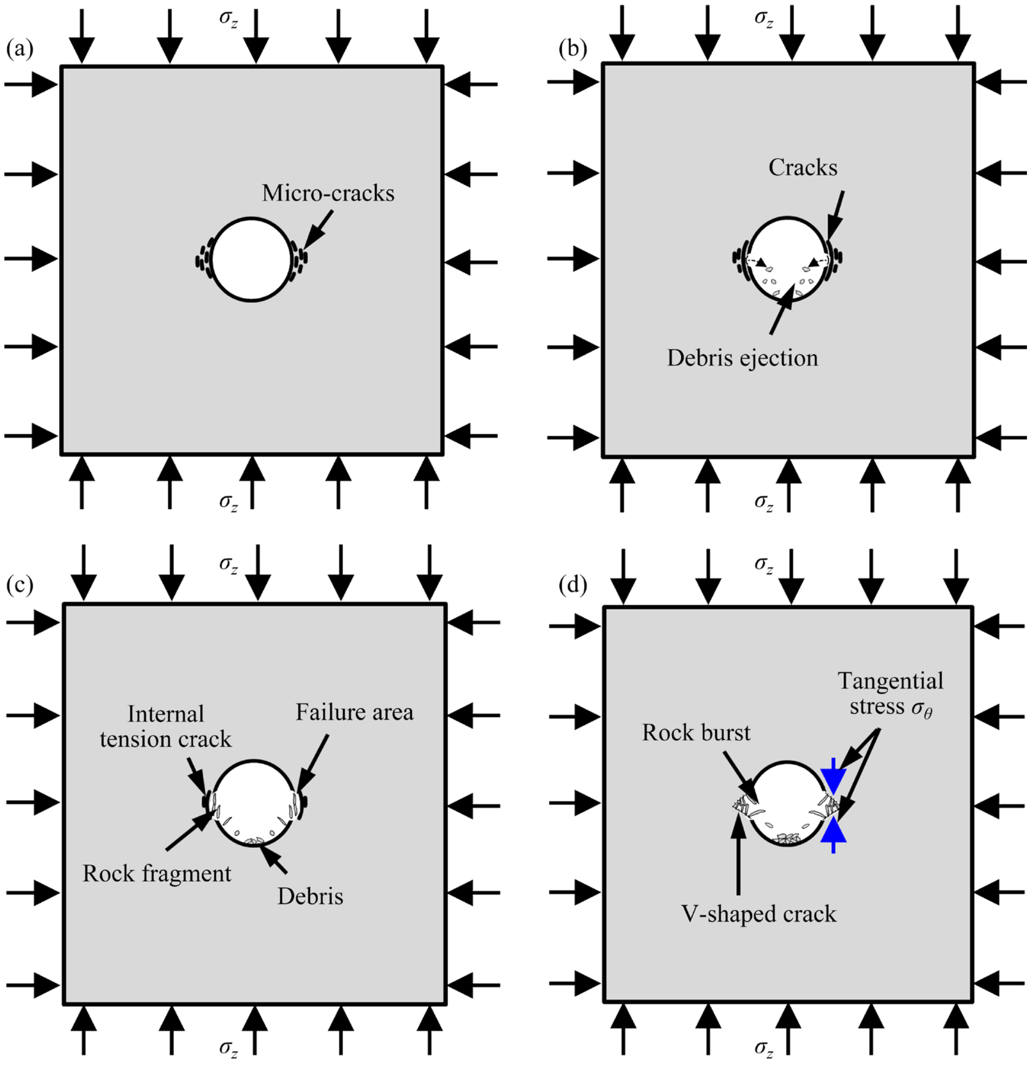

Fig. 5 Failure mechanism of rockburst: (a) Quiet period; (b) Crack propagation period; (c) Rock fragment exfoliation period; (d) Rockburst period

stress conditions are investigated in this section, and the failure processes of the holed specimens subjected to a constant maximum principal stress (σ_z=100 MPa) are presented in Fig. 6. Failure near the circular hole decreases with an increase in the horizontal principal stresses, including the principal stresses in the x and y directions. In particular, no evident failure occurs when the stress in the x direction increases to be larger than 30 MPa, as shown in Figs. 6(e) and (f). This indicates that increasing the stress along the axial direction of the hole can strengthen the stability to a certain extent. In other words, a tunnel buried at a great depth can increase the stability of the surrounding rock, and the axial direction of the underground tunnel in deep hard rock should be parallel to the direction of the maximum horizontal principal stress.

Furthermore, the horizontal principal stress difference has a significant influence on the failure characteristics of the specimen, as shown in Fig. 3 and Figs. 6(a−d), where low-stress (Figs. 6(a) and (b)) and high-stress (Figs. 6(c) and (d)) conditions are considered. The failure level of the surrounding rock increases gradually as the horizontal principal stress difference increases in the order of 5→10→20→30 MPa, and the failure modes of the specimen change from spalling to rockburst with the increase in horizontal stresses. Additionally, a larger horizontal stress difference can induce a deeper V-shaped crack on both sidewalls of the circular hole, as shown in Fig. 4. Therefore, the failure of the rock surrounding the circular tunnel increases with the increase in the horizontal stress difference.

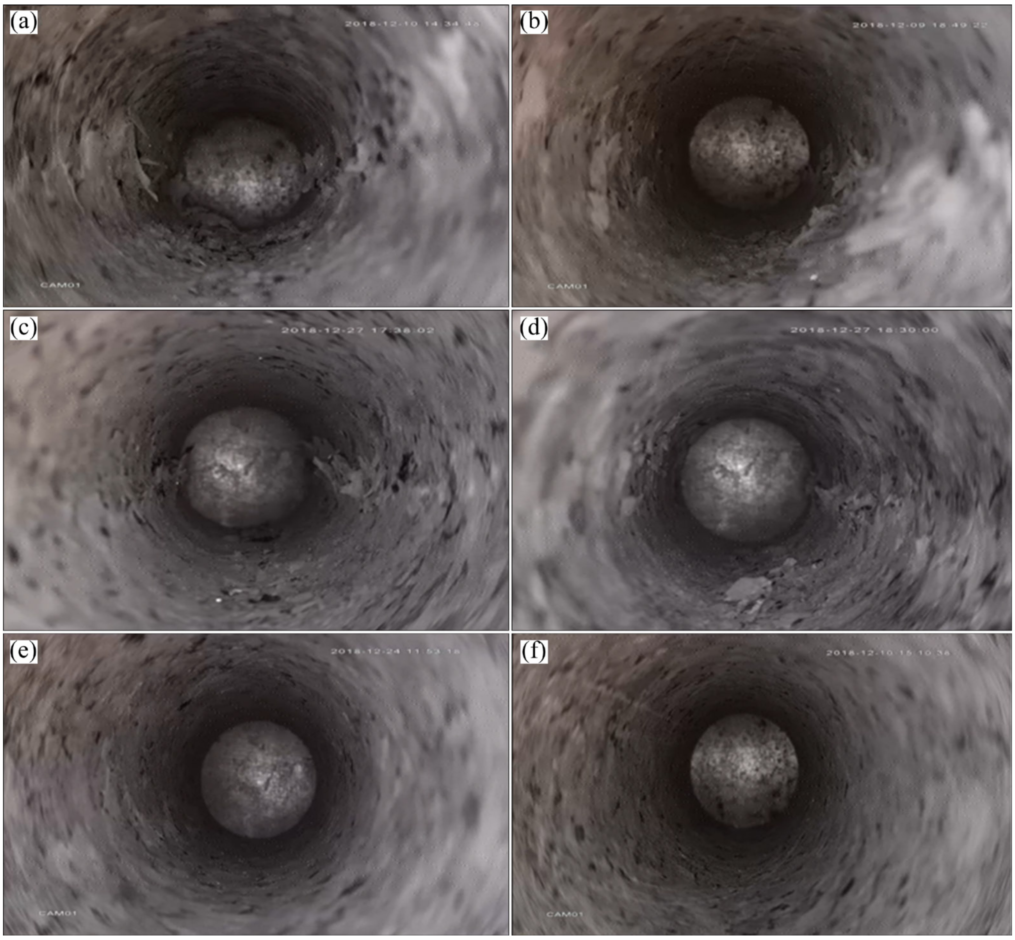

Fig. 6 Failure characteristics near sidewalls of specimens at σ_z=100 MPa: (a) 5-10-100; (b) 10-20-100; (c) 10-30-100; (d) 10-40-100; (e) 30-40-100; (f) 50-40-100

This is because increasing the horizontal stress difference can promote the accumulation of elastic strain energy in the surrounding rock within the scope of a certain stress and decrease the deviation stress. In general, the decreased deviation stress can further weaken the shear stress concentration in the surrounding rock and enhance the accumulation of strain energy in the vicinity of the underground tunnel if the maximum principal stress is loaded along the direction perpendicular to the tunnel axis and middle principal stress to accumulate more energy for serious rock failure. Similarly, decreasing the horizontal stress difference by increasing the stress along the tunnel axis can increase the stability of the surrounding rock, as shown in Figs. 6(e) and (f). In this case, a large amount of elastic strain energy is accumulated in the surrounding rock, which can lead to a violent rockburst near the tunnel wall if the maximum principal stress increases to meet the requirement of rock failure, as shown in Fig. 3(c).

3.3 Stress of hole sidewalls

Based on Kirsch theory, the tangential stress σ_θ near the sidewall of a circular hole can be calculated using the following formula [31]:

$$\sigma_\theta = \frac{\sigma_y + \sigma_z}{2}\left(1+\frac{R^2}{r^2}\right) - \frac{\sigma_y - \sigma_z}{2}\left(1+\frac{3R^4}{r^4}\right)\cos(2\theta) \tag{1}$$

where θ is the angle with the horizontal phane, R is the tunnel radius, r is the coordinate radius, and σ_y is the horizontal stress in the y direction.

When r=R, the tangential stress σ_θ near the hole wall is

$$\sigma_\theta = [1-2\cos(2\theta)]\sigma_y + [1+2\cos(2\theta)]\sigma_z \tag{2}$$

The tangential stress σ_θ near the middle sidewalls (θ=0° and θ=180°) of the hole is calculated when the first through crack occurs, and the results are presented in Table 2, where σ_{z0} is the stress at the beginning of failure. The initial failure stress increases with the increase of the horizontal stress, which is consistent with the conclusion obtained in the previous section; increasing the horizontal stress can enhance the stability of the tunnel. Furthermore, the calculated tangential stress under different stress conditions is larger than the average laboratory UCS value (98 MPa), that is, the ratio of the tangential stress at the initial failure of the specimen to the laboratory UCS is greater than 1. Combined with the findings in Fig. 4, a larger horizontal stress can induce a stronger rockburst in the surrounding rock if the stress increases sufficiently to damage the tunnel.

The normalized mean stress (σ_m) and normalized deviatoric stress (σ_d) can be calculated as [32]:

$$\sigma_m = \frac{\sigma_z + \sigma_y}{2\sigma_c} \tag{3}$$

$$\sigma_d = \frac{\sigma_z - \sigma_y}{2\sigma_c} \tag{4}$$

where σ_c is the USC of the holed rock specimen.

Table 2 Stresses on both sidewalls of hole

Specimen	σ_x/ MPa	σ_y/ MPa	σ_{z0}/ MPa	σ_z/ MPa	σ_θ/ MPa	σ_θ/σ_c
5-10-σ_z	5	10	52	105	146	1.21
10-20-σ_z	10	20	56	110	148	1.22
10-30-σ_z	10	30	63	131	159	1.31
10-40-σ_z	10	40	68	136	164	1.36
30-40-σ_z	30	40	97	163	200	1.65
50-40-σ_z	50	40	103	180	269	2.74
0-0-σ_z	0	0	−	60	−	−

Utilizing Eqs. (3) and (4), σ_m and σ_d at the beginning of failure (T_1), 70% of the maximum stress in the z direction (T_2), and the maximum stress in the z direction (T_3) under different stress states were calculated, and the results are presented in Table 3. The obtained results are consistent with the findings in Section 3.2. Furthermore, based on Ref. [32], the relationship between the failure mode of the unsupported circular tunnel and the far-field stress state in this experiment is shown in Fig. 7, where type I is ear-shaped, type II is ring-shaped, and type III is butterfly-shaped. Failures around the circular tunnel are mainly ear-shaped and butterfly-shaped, and the initial failure is always distributed near the sidewalls of the circular hole, that is, the position perpendicular to the maximum principal stress. As the maximum principal stress increases, the failure gradually extends in the other directions of the hole and a butterfly-shaped failure is formed. In addition, the butterfly-shaped failure of Specimens 5-10-σ_z, 10-20-σ_z, and 50-40-σ_z is earlier than that of Specimens 10-30-σ_z, 10-40-σ_z, and 30-40-σ_z, indicating that Specimens 5-10-σ_z,

Table 3 Calculated results of three failure states of sidewall under different stress conditions

Specimen	Stage	σ_z/MPa	σ_m	σ_d	$K=\sigma_z/\sigma_y$	Failure type
5-10-σ_z	T_1	52.0	0.256	0.174	0.19	I
	T_2	73.5	0.345	0.262	0.14	III
	T_3	105.0	0.475	0.393	0.095	III
10-20-σ_z	T_1	56.0	0.314	0.149	0.36	I
	T_2	77.0	0.401	0.236	0.26	III
	T_3	110.0	0.573	0.372	0.18	III
10-30-σ_z	T_1	63.0	0.384	0.136	0.47	I
	T_2	91.7	0.503	0.255	0.33	I
	T_3	131.0	0.665	0.417	0.23	III
10-40-σ_z	T_1	68.0	0.456	0.116	0.59	I
	T_2	95.2	0.559	0.228	0.42	I
	T_3	136.0	0.727	0.397	0.29	III
30-40-σ_z	T_1	97.0	0.5661	0.236	0.41	I
	T_2	114.1	0.638	0.306	0.35	I
	T_3	163.0	0.839	0.508	0.25	III
50-40-σ_z	T_1	108.0	0.612	0.281	0.37	I
	T_2	133.0	0.715	0.384	0.30	III
	T_3	190.0	0.950	0.620	0.21	III

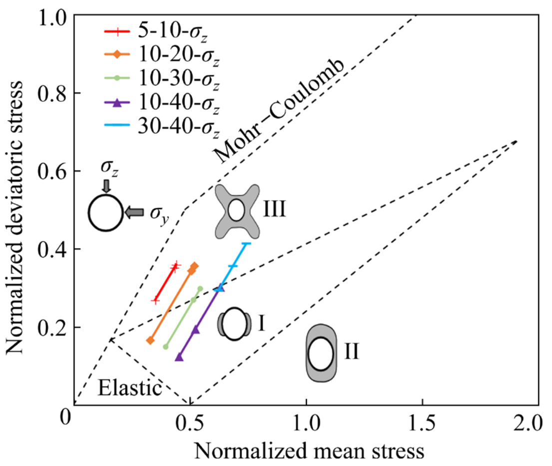

Fig. 7 Relationship between failure modes and far-field stress state for unsupported circular opening [32]

10-20-σ_z, and 50-40-σ_z are more prone to shear failure. In other words, shallow-buried and extremely deep tunnels are more prone to shear failure than medium-buried tunnels. This is because the deviation stresses in the shallow-buried and extremely deep areas are larger than those in the medium-buried areas owing to the difference in in situ stress.

4 Numerical simulation

In the previous sections, the failure characteristics and stress distributions around circular holes under different stress conditions were obtained by real triaxial experiments. However, the energy distributions and variations during the loading process could not be obtained from the experimental data. Therefore, in the following sections, numerical simulation was used to further study the energy distributions in the surrounding rock under 3D stress.

4.1 Description and verification of material model

To verify the feasibility of the parameters obtained from experiments in numerically characterizing the properties of rock material, the uniaxial compression test of the holed specimens used in the experiments was numerically reproduced based on the explicit program ABAQUS. A numerical model of the same size (100 mm × 100 mm × 100 mm) as the experiment was established using ABAQUS. A fine grid of elements was used to increase the accuracy of the results in the vicinity of the circular hole, and the grid size increased with the increase in the distance from the hole surface. To maintain consistency with laboratory tests, the physic-mechanical parameters used in numerical simulations were those of the granite specimens as follows: density (ρ) 2650 kg/m^3, Young's modulus (E) 31.5 GPa, Poisson's ratio (υ) 0.25, UCS 98 MPa, cohesion (c) 33.46 MPa, and friction angle (φ) 36°. The uniaxial compressive strength of holed Specimen 0-0-σ_z was 60 MPa.

The strength characteristics of the rock specimens were simulated using the Mohr–Coulomb softening model. The strain-softening parameters of the model are listed in Table 4. The same loading method used in the experiments was adopted for the numerical simulations. The failure modes and strain–stress curves of the holed specimens obtained in the uniaxial compression experiment and numerical simulation are shown in Fig. 8. The results obtained in the numerical simulations are consistent with the experimental results, including Young's modulus, yield strength, peak strength, and failure modes. This indicates that the Mohr–Coulomb model can be used to simulate the failure characteristics of holed specimens. The strains corresponding to the peak stress obtained in experiments are larger than those obtained in numerical simulations. In general, a real rock specimen contains many natural microfractures, which are compacted under an external force. However, the numerical model comprises elastic finite elements; its deformation changes linearly with external force, and there is no pore compaction. Thus, the deformation of the real rock specimen is greater than that of the numerical specimen.

Table 4 Strain-softening parameters of model

Cohesion yield stress/MPa	Plastic shear strain
35.46	0
33.00	0.0035
30.00	0.0080
25.00	0.0170
20.00	0.0280
15.00	0.0410
10.00	0.0580
5.00	0.0800
0.01	0.1100

4.2 Distribution of energy around circular hole under different stress conditions

In this section, the distribution of energy around the circular holes under different stress states was numerically investigated to reveal the failure mechanism of the surrounding rocks. To maintain consistency with the experimental process, displacement constraints were applied to the boundary of the specimen opposite to the loading face. The stress was loaded on the specimen faces from the x, y, and z directions in two steps. The first step was to initialize the stress conditions and create the model in the initial stress state. Then, the horizontal stress was maintained constant, and the stress in the z direction was increased until the model was damaged. Using the same loading process, triaxial compression experiments of Specimens 10-20-σ_z, 10-40-σ_z, and 50-40-σ_z were simulated successively.

To evaluate the energy around the circular hole during loading processes, the energy distribution characteristics in the surrounding rock of the circular holes in the initial stage, elastic stage, and plastic stage, namely, Stages *A*, *B*, and *C*, are presented in Fig. 9. The initial stage indicates that the specimen is only loaded with principal stresses

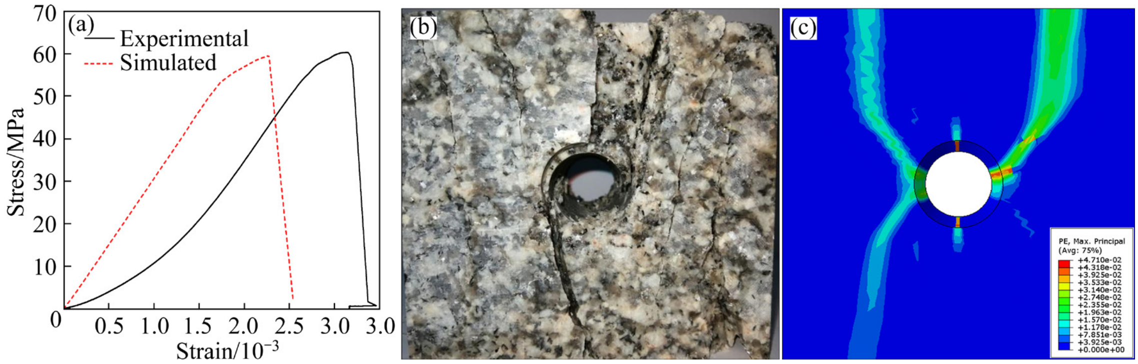

Fig. 8 Comparison of experimental and numerical results: (a) Strain–stress curves; (b) Failure modes obtained in experiment; (c) Failure modes obtained in simulation

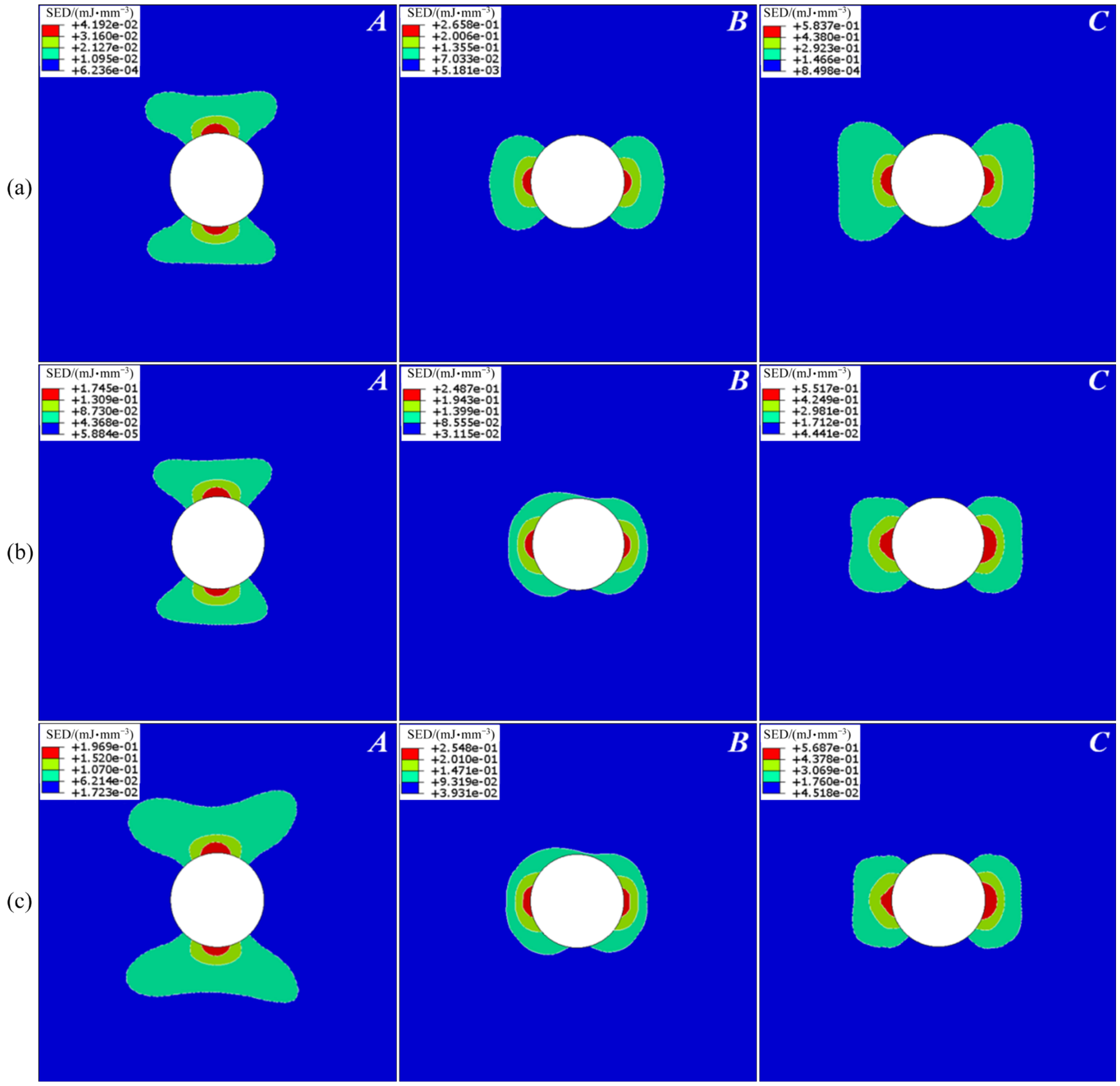

Fig. 9 Distribution of strain energy density (SED) around hole under different stress conditions: (a) 10-20-σ_z; (b) 10-40-σ_z; (c) 50-40-σ_z

in the x and y directions, and the distribution of SED in the surrounding rock is used to express the energy distributions around the circular hole. Figure 9 shows that the SED is mainly distributed near the top and bottom parts of the circular hole in a butterfly shape in the initial stage, and the maximum SED values of Specimens 10-20-σ_z, 10-40-σ_z, and 50-40-σ_z are 0.0419, 0.175 , and 0.197 mJ/mm^3, respectively. The larger principal stress in the x and y directions can induce a greater SED in the initial stage, and a high SED is mainly distributed near the inner wall of the circular hole. As the distance to the hole wall increases, the SED value decreases gradually, while the distribution areas show an evident increase. As the principal stress in the z direction is loaded on the sample and increases, the SED near the hole wall increases gradually, and the distribution of the high SED around the circular hole migrates from the top and bottom parts to its sidewalls. The maximum and minimum SED values are always distributed at both sidewalls and in the longitudinal direction of the hole, respectively. In contrast to the failure characteristics of the surrounding rock obtained from the experiments, the failure of the surrounding rock always occurs at positions with high SED, which is mainly caused by compressive stress concentration. The maximum SED values of Specimen 10-20-σ_z, 10-40-σ_z, and 50-40-σ_z at failure are 0.584, 0.552, and 0.568 mJ/mm^3, respectively. Evidently, the SED value of specimen 10-20-σ_z at failure is larger than the others because the higher the initial stress of the specimens is, the more evident the damage to the surrounding rock around the circular hole at failure is, and thus, the smaller the residual strain energy in the surrounding rock is.

4.3 Influence of horizontal stress on distribution of SED near hole

As shown in Fig. 9, the distribution shape of SED in different stages is related to the horizontal stress conditions, that is, the stress in the x and y directions. To investigate the influence of horizontal stresses on the distribution of SED around the circular hole, the stress in the direction of the maximum principal stress (z direction) was maintained at 100 MPa, and the stresses in the x and y directions were changed to check the distribution of SED around the circular hole under different stress ratio coefficients. The specific simulation schemes are presented in Table 5, where K_1 and K_2 are the stress ratios in the z direction to the x and y directions, respectively.

Table 5 Simulation scheme showing influence of side pressure coefficient

Specimen	σ_z/MPa	σ_y/MPa	σ_x/MPa	$K_1(=\sigma_z/\sigma_x)$
30-50-100	100	50	30	3.3
50-50-100	100	50	50	2.0
100-50-100	100	50	100	1.0
Specimen	σ_z/MPa	σ_y/MPa	σ_x/MPa	$K_2(=\sigma_z/\sigma_y)$
10-30-100	100	30	10	3.3
10-50-100	100	50	10	2.0
10-100-100	100	100	10	1.0

Figure 10 shows the distribution characteristics of SED in the surrounding rock with different stress ratio coefficients, K_1 and K_2. An evident SED concentration area is formed in the surrounding rock, in particular, the sidewalls of the hole under different K_1, and the maximum and minimum SED values always occur at the sidewalls, top, and bottom parts of the hole, which is similar to that in Fig. 9. This means that the failure of the surrounding rock, including spalling and rockburst, is the release process of the compressive strain energy. In addition, the distribution characteristics of the SED around the hole under different K_1 values are similar, shown as an ear shape. However, the SED value of the surrounding rock decreases slightly with decreasing K_1. As the stress ratio coefficient K_2 increases, the SED around the hole decreases, and their distribution characteristics change from butterfly-shaped to ring-shaped. In contrast to the cases under different K_1, the decreasing K_2 has a greater influence on the SED distribution around the circular hole. Therefore, the large stress within the cross-section of an underground tunnel can pose a greater threat to its stability than the stress along the axial direction of the tunnel, which is consistent with the results obtained by LI et al [33] and SI et al [14]. In addition, increasing the stress in the x direction can decrease the SED in the surrounding rock and strengthen its stability accordingly. This is because increasing the stress in the x direction can restrict the deformation of the surrounding rock near the

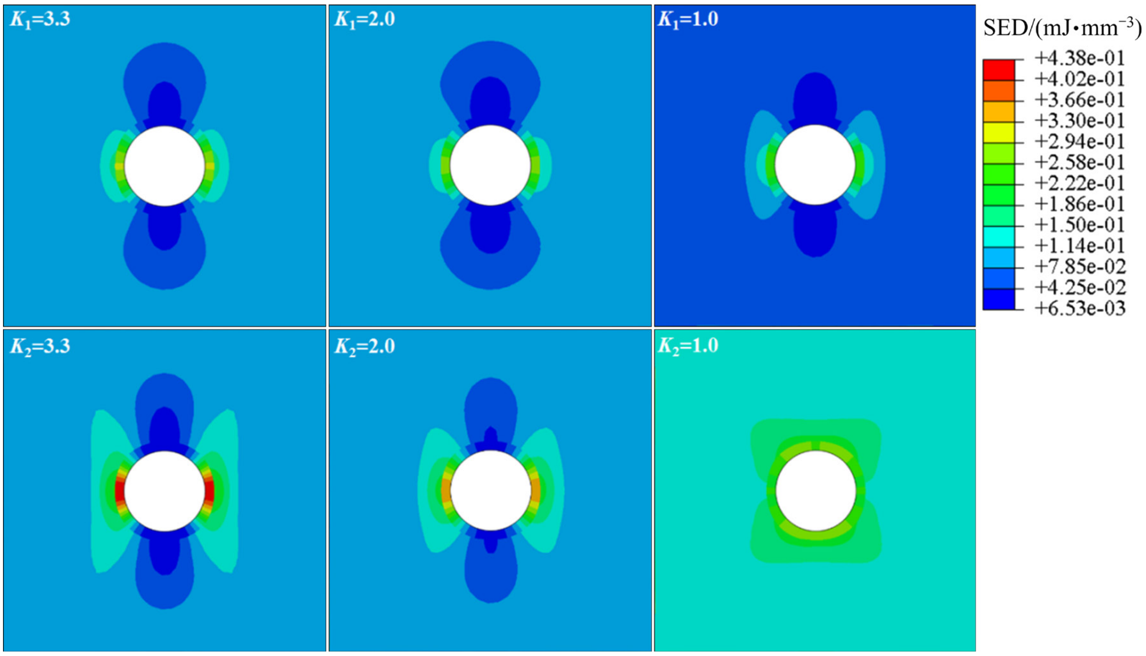

Fig. 10 Distribution of SED in surrounding rock of holed specimens with different K_1 and K_2

tunnel wall if the stresses are loaded along the cross-section of the tunnel, and the small difference in the stresses within the cross-section of the tunnel (σ_y and σ_z) can decrease the shear deformation in the surrounding rock.

5 Discussion

The numerical simulation results demonstrate that the distribution characteristic of SED around circular holes is influenced by the horizontal stresses, including the stress perpendicular to the cross-section of the tunnel and the stress within the cross-section. The latter has a greater influence on the distribution characteristics of SED, deformation, and failure around the tunnel. In general, the serious deformation and SED are mainly distributed near the position perpendicular to the maximum principal stress. The relationship between the stress ratio coefficient and the failure around the circular hole is shown in Fig. 11, where σ_z is the maximum principal stress. The grey V-shaped area is considered to be the compressive stress concentration area around the circular hole. From this point, lateral deformation will occur in the surrounding rock owing to Passion's effect on the rock material when the compressive stress is concentrated near the sidewalls of the tunnel, which can further evoke tensile failure of the sidewalls along the radial direction of the tunnel. In general, the compressive stress concentration around a circular tunnel is greater than the tensile stress concentration. Therefore, along the radial direction of the tunnel, the surrounding rock in the compressive stress concentration areas is more prone to tensile failure than that in the tensile stress concentration area, as presented in Fig. 3 and Fig. 5. The stress concentration and SED gradually decrease with increasing distance from the sidewalls, which can also be used to explain the V-shaped failure emerging in the tunnel sidewalls. From the perspective of energy, a large amount of compressive strain energy is accumulated in the compressive stress concentration areas of the tunnel, and the maximum SED is generally distributed on the tunnel surface, as presented in Fig. 9 and Fig. 10. In this case, the failure that occurs in the compressive stress concentration areas can induce a rapid release of strain energy, and the failure of the surrounding rock shows an evident rockburst, as presented in Fig. 3.

The maximum SED in the surrounding rock decreases with the increase in horizontal stress, including the stress in the x and y directions, and the variation of stresses in the cross-section of circular tunnels has a greater influence on the distribution of SED around the tunnel than that perpendicular to the cross-section, as shown in Fig. 10. Thus, it can

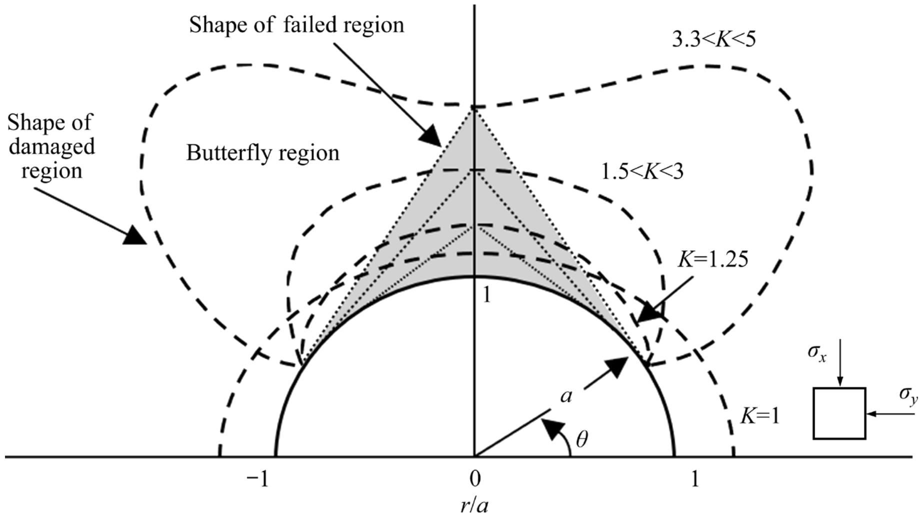

Fig. 11 Failure characteristics of surrounding rock with different side pressure coefficients

be concluded that the energy accumulation in the surrounding rock can be restrained by increasing the horizontal stress, which is consistent with the experimental results in Section 3.2. In addition, as the horizontal stress increases, the rockburst near the sidewalls first increases and then decreases, as shown in Fig. 4. Based on the results presented in Fig. 11, the increasing horizontal stresses restrain the deformation of the surrounding rock, particularly in the vicinity of the tunnel wall. In addition, plastic deformation occurs in rock specimens when the stress state is greater than the yield stress, which can further decrease the strain energy in the surrounding rock and intensity of the surrounding rock failure. Moreover, the SED distribution around the circular tunnel changes from butterfly-shaped to ear-shaped and then to ring-shaped with variations in the side pressure coefficients.

6 Conclusions

(1) The spalling processes can be divided into four periods: quiet, debris ejection, crack propagation, and rock fragment exfoliation. Spalling failure occurs in a tunnel under low-stress conditions, whereas rockburst occurs near the tunnel under high-stress conditions, and its failure processes include the quiet period, debris ejection period, rock fragment exfoliation period, and rockburst period.

(2) When the maximum principal stress (σ_z) is fixed, increasing the horizontal stresses (σ_x and σ_y) reduces the degree of damage to the surrounding rock. However, when the maximum principal stress continues to increase and is greater than the yield stress of the surrounding rock, the intensity of the rockburst is reduced, and the high horizontal stresses can provide energy for the rockburst. Reducing the horizontal stress difference can reduce the rockburst intensity.

(3) High and low SED are always distributed near the sidewalls of the circular tunnel and along the direction of the maximum principal stress. Tunnels under low-stress conditions can form a larger SED distribution area in the surrounding rock at failure than those under high-stress conditions. Distributions of SED around circular tunnels will decrease with increasing stress perpendicular to the cross-section of the tunnel and stress within the cross-section.

Acknowledgments

This research was supported by the National Natural Science Foundation of China (No. 12072376) and the Fundamental Research Funds for the Central Universities of Central South University, China (No. 2020zzts708).

References

[1] YIN Zhi-qiang, LI Xi-bing, JIN Jie-fang, HE Xian-qun, DU Kun. Failure characteristics of high stress rock induced by impact disturbance under confining pressure unloading [J]. Transactions of Nonferrous Metals Society of China, 2012, 22(1): 175−184.

[2] ZHOU Hui, LU Jing-jing, XU Rong-chao, ZHANG Chuan-qing, MENG Fan-zhen. Critical problems of study of slabbing failure of surrounding rock in deep hard rock tunnel and research progress [J]. Rock and Soil Mechanics, 2015, 36(10): 2737−2749. (in Chinese)

[3] WU Hao, ZHAO Guo-yan, MA Shao-wei. Failure behavior of horseshoe-shaped tunnel in hard rock under high stress: Phenomenon and mechanisms [J]. Transactions of Nonferrous Metals Society of China, 2022, 32(2): 639−656.

[4] ZHAO Hua-tao, TAO Ming, LI Xi-bing, HONG Zhi-xian, ZHAO Rui, CAO Wen-zhuo. Experimental investigation on dynamic mechanical properties and fracture evolution behavior of the underground openings with excavation damaged zones [J]. International Journal of Damage Mechanics, 2022, 31(10): 1533−1561.

[5] LONG Yi, LIU Jian-po, LEI Gang, SI Ying-tao, ZHANG Chang-yin, WEI Deng-cheng, SHI Hong-xu. Progressive fracture processes around tunnel triggered by blast disturbances under biaxial compression with different lateral pressure coefficients [J]. Transactions of Nonferrous Metals Society of China, 2020, 30(9): 2518−2535.

[6] TAO Ming, ZHAO Hua-tao, LI Zhan-wen, ZHU Jian-bo. Analytical and numerical study of a circular cavity subjected to plane and cylindrical P-wave scattering [J]. Tunnelling and Underground Space Technology, 2020, 95: 103143.

[7] ZHAO Hua-tao, TAO Ming, LI Xi-bing, MIKADA H, XU Shi-bo. Influence of excavation damaged zone on the dynamic response of circular cavity subjected to transient stress wave [J]. International Journal of Rock Mechanics and Mining Sciences, 2021, 142: 104708.

[8] MA Dan, DUAN Hong-yu, ZHANG Ji-xiong. Solid grain migration on hydraulic properties of fault rocks in underground mining tunnel: Radial seepage experiments and verification of permeability prediction [J]. Tunnelling and Underground Space Technology, 2022, 126: 104525.

[9] KAISER P K, CAI Ming. Design of rock support system under rockburst condition [J]. Journal of Rock Mechanics and Geotechnical Engineering, 2012, 4(3): 215−227.

[10] LI Shao-jun, FENG Xia-ting, LI Zhan-hai, CHEN Bing-rui, ZHANG Chuan-qing, ZHOU Hui. In situ monitoring of rockburst nucleation and evolution in the deeply buried tunnels of Jinping II hydropower station [J]. Engineering Geology, 2012, 137: 85−96.

[11] QIAN Qi-hu. Challenges faced by underground projects construction safety and countermeasures [J]. Chinese Journal of Rock Mechanics and Engineering, 2012, 31(10): 1945−1956. (in Chinese)

[12] MARTINI C D, READ R S, MARTINO J B. Observations of brittle failure around a circular test tunnel [J]. International Journal of Rock Mechanics and Mining Sciences, 1997, 34(7): 1065−1073.

[13] FENG Xia-ting, XU Hong, QIU Shao-jun, YANG Cheng-xiang, GUO Hao-sen, CHEN Yuan, GAO Yao-hui. In situ observation of rock spalling in the deep tunnels of the China Jinping Underground Laboratory (2400 m depth) [J]. Rock Mechanics and Rock Engineering, 2018, 51(4): 1193−1213.

[14] SI Xue-feng, HUANG Lin-qi, LI Xi-bing, MA Chun-de, GONG Feng-qiang. Experimental investigation of spalling failure of D-shaped tunnel under three-dimensional high-stress conditions in hard rock [J]. Rock Mechanics and Rock Engineering, 2021, 54(6): 3017−3038.

[15] VAZAIOS I, VLACHOPOULOS N, DIEDERICHS M S. Mechanical analysis and interpretation of excavation damage zone formation around deep tunnels within massive rock masses using hybrid finite–discrete element approach: Case of Atomic Energy of Canada Limited (AECL) Underground Research Laboratory (URL) test tunnel [J]. Canadian Geotechnical Journal, 2019, 56(1): 35−59.

[16] READ R S. 20 years of excavation response studies at AECL’s Underground Research Laboratory [J]. International Journal of Rock Mechanics and Mining Sciences, 2004, 41(8): 1251−1275.

[17] JACOBSSON L, APPELQUIST K, LINDKVIST J E. Spalling experiments on large hard rock specimens [J]. Rock Mechanics and Rock Engineering, 2015, 48(4): 1485−1503.

[18] ZHAO Hua-tao, TAO Ming, LI Xi-bing, CAO Wen-zhuo, WU Cheng-qing. Estimation of spalling strength of sandstone under different pre-confining pressure by experiment and numerical simulation [J]. International Journal of Impact Engineering, 2019, 133: 103359.

[19] HUANG Lin-qi, WANG Jun, MOMENI A, WANG Shao-feng. Spalling fracture mechanism of granite subjected to dynamic tensile loading [J]. Transactions of Nonferrous Metals Society of China, 2021, 31(7): 2116−2127.

[20] KENETI A, SAINSBURY B A. Review of published rockburst events and their contributing factors [J]. Engineering Geology, 2018, 246: 361−373.

[21] DYSKIN A V, GERMANOVICH L N. Model of rockburst caused by cracks growing near free surface [J]. Rockbursts and Seismicity in Mines, 1993, 93: 169−175.

[22] ORTLEPP W D, STACEY T R. Rockburst mechanisms in tunnels and shafts [J]. Tunnelling and Underground Space Technology, 1994, 9(1): 59−65.

[23] HE Man-caho, XIA Hong-man, JIA Xue-na, GONG Wei-li, ZHAO Fei, LIANG Kang-yuan. Studies on classification, criteria and control of rockbursts [J]. Journal of Rock Mechanics and Geotechnical Engineering, 2012, 4(2): 97−114.

[24] GONG Feng-qiang, SI Xue-feng, LI Xi-bing, WANG Shan-yong. Experimental investigation of strain rockburst in circular caverns under deep three-dimensional high-stress conditions [J]. Rock Mechanics and Rock Engineering, 2019, 52(2): 1459−1474.

[25] ZHU W C, LI Z H, ZHU L, TANG C A. Numerical simulation on rockburst of underground opening triggered by dynamic disturbance [J]. Tunnelling and Underground Space Technology, 2010, 25(5): 587−599.

[26] TAO Ming, ZHAO Hua-tao, MOMENI A, WANG Yi-qing, CAO Wen-zhuo. Fracture failure analysis of elliptical hole bored granodiorite rocks under impact loads [J]. Theoretical and Applied Fracture Mechanics, 2020, 107: 102516.

[27] DU Kun, TAO Ming, LI Xi-bing, ZHOU Jian. Experimental study of slabbing and rockburst induced by true-triaxial unloading and local dynamic disturbance [J]. Rock Mechanics and Rock Engineering, 2016, 49(9): 3437−3453.

[28] GONG Feng-qiang, LUO Yong, LI Xi-bing, SI Xue-feng,

TAO Ming. Experimental simulation investigation on rockburst induced by spalling failure in deep circular tunnels [J]. Tunnelling and Underground Space Technology, 2018, 81: 413−427.

[29] STEPHANSSON O, SÄRKKÄ P, MYRVANG A. State of stress in fennoscandia [C]//International Symposium on Rock Stress and Rock Stress Measurements. Stockholm, 1986: 21−32.

[30] HOEK E, BROWN E T. Practical estimates of rock mass strength [J]. International Journal of Rock Mechanics and Mining Sciences, 1997, 34(8): 1165−1186.

[31] HUBBERT M K, WILLIS D G. Mechanics of hydraulic fracturing [J]. Transactions of the AIME, 1957, 210(1): 153−168.

[32] MARTIN C D, KAISER P K, MCCREATH D R. Hoek−Brown parameters for predicting the depth of brittle failure around tunnels [J]. Canadian Geotechnical Journal, 1999, 36(1): 136−151.

[33] LI Xi-bing, DU Kun, LI Di-yuan. True triaxial strength and failure modes of cubic rock specimens with unloading the minor principal stress [J]. Rock Mechanics and Rock Engineering, 2015, 48(6): 2185−2196.

不同三维应力条件下硬岩巷道围岩的破坏特征及能量分布

陶明[1]，赵瑞[1]，赵华涛[1]，王一清[1]，曹文卓[2]，王少锋[1]

1. 中南大学 资源与安全工程学院，长沙 410083；
2. Royal School of Mines, Imperial College, London, United Kingdom

摘　要：为了研究开挖巷道围岩在不同三维应力条件下的破坏特征，采用 TRW3000 岩石真三轴电液伺服试验系统对含圆孔花岗岩试件进行三轴加载试验，并利用微型高清摄像系统实时记录圆孔附近的失效过程。结果表明，低应力条件下，圆孔内壁主要发生层裂破坏；高应力条件下，圆孔周边主要发生岩爆破坏。增加水平方向的应力可以抑制围岩发生岩爆。进一步数值模拟不同应力条件下圆孔周边的应变能密度(SED)演化过程。模拟结果表明，随着水平应力的增加，圆孔周边的 SED 分布逐渐减小；圆孔周边 SED 分布与实验记录的损伤分布基本一致，主要表现为蝶形、耳形和环形分布。

关键词：深部硬岩巷道；真三轴试验；水平应力差；破坏特征；能量分布

(Edited by Wei-ping CHEN)